DETC2019-98215

FROM SCAN STRATEGY TO MELT POOL PREDICTION: A NEIGHBORING-EFFECT MODELING METHOD

Zhuo Yang[1], Lu Yan[2, *], Ho Yeung[2], Sundar Krishnamurty[1]

University of Massachusetts Amherst[1]
Department of Mechanical and Industrial Engineering
Amherst, MA 01003

National Institute of Standards and Technology[2]
Engineering Laboratory
Gaithersburg, MD 20899

ABSTRACT

The quality of AM built parts is highly correlated to the melt pool characteristics. Hence melt pool monitoring and control can potentially improve AM part quality. This paper presents a neighboring-effect modeling method (NBEM) that uses scan strategy to predict melt pool size. The prediction model can further assist in scan strategy optimization and real-time process control. The structure of the proposed model is formulated based on the physical principles of melt pool formation, while experimental data is used to identify the optimal coefficients. Compared to the traditional power-velocity prediction models, NBEM model introduces the cumulative neighboring-effect factors as additional input variables. These factors represent the neighborhood impact of scan path on the focal point melt pool formation from time and distance perspective. Two experiments use different scan strategies to collect in-situ measurements of melt pool size for model construction and validation. By introducing the neighboring-effect factors, the global Normalized Root Mean Square Error (NRMSE) is improved from around 0.10 to 0.08. More importantly, the local NRMSE of irregular melt pool area prediction is improved to around 0.15 for more than 50% improvement. The case studies verify that the proposed method can predict the melt pool variations by seamlessly integrating scan strategy considerations.

1. INTRODUCTION

In laser powder bed fusion (L-PBF) additive manufacturing (AM), thin layers of powder are applied to a build plate and a laser source is used to fuse the powder to the desired geometry.

This process is repeated layer by layer until the 3D part is built [1]. Melt pool formation is an important AM subprocess that involves various complex physical phenomena such as phase change, thermal conduction, and fluid dynamics. Laser power and scan velocity are reported to have a significant impact on the melt pool size [2, 3].

Recent studies indicate that melt pool shape and size could significantly affect the material properties of AM parts. It is largely accepted that the porosity in L-PBF parts can be attributed to improper melt pool formation such as lack of fusion and trapped gas [4]. Abnormal melt pools closely relate to AM part defects such as pores and keyholes [5-7]. Hence, ability to accurately characterize melt pool area can improve build pedigree toward ultimate prediction of material properties and proactive part qualification.

Many processing parameters are identified with effects on melt pool size and shape. Empirical studies indicate that those energy density related processing parameters, such as laser power, scan velocity, and hatch spacing, have substantial impacts on melt pool formation. Higher laser power or lower scan velocity results in larger melt pool size when other conditions remain the same [8-10]. Melt pool formation is also affected by environmental conditions such as gas nature and preheating temperature [11]. Preheating temperature has material dependent influences on part density, internal stress, microstructure and crack formation[12]. Overhang may introduce more uncertainties to melt pool size according to empirical studies [8]. Understanding the influence of these

---

* Contact author: yan.lu@nist.gov

parameters on melt pool formation can potentially improve AM part quality.

Predictive models provide an efficient and inexpensive way to evaluate AM processes. Both physics-based and statistics-based modeling methods have been widely used in L-PBF. The physics-based modeling methods rely on physical knowledge to predict melt pool size of L-PBF parts. For example, finite element analysis (FEA) models use thermal analysis to simulate the temperature distribution of a melt pool and the surrounding powders to derive the melt pool width [13-15]. Computational fluid dynamics (CFD) models focus on resolving the thermal-fluid flow behaviors of individual powder particles, which provides detailed information at particle level [6, 16]. CFD and FEA models assume little model simplifications to produce high fidelity results. Comparatively, data-driven methods model an L-PBF process as a black-box, ignoring the inherent complex phenomena and dynamic nature in the process. Melt pool prediction using metamodeling techniques, aka surrogate modeling, relies on data only to construct a relationship between process parameters and melt pool characteristics without incorporating physical principles. Usually, this technique is used for fast/low-cost AM prediction [8, 17].

Existing data-driven melt pool prediction models commonly assume over-simplified scan patterns, e.g., using constant laser power, scan speed and hatch distance. However, current commercial AM machines usually automatically generate scan strategies based on the imported 3D models, which could be very complicated [18]. It is unclear the impact of scan strategy on AM part quality, especially the parameter settings between sectors. Since the scan paths and process parameters of most commercial systems are black boxes to the end users, this study uses an open additive manufacturing testbed and applies complex scan strategies to identify the relationship between scan strategy and melt pool geometry. The testbed used in this study can import G-Code and transform it into a sequence of Galvo scanner positions and laser power settings, which are usually not fully available from any AM commercial machine. However, the modeling approach can be adopted by AM machine manufacturers to characterize, calibrate their systems and configure the best scan strategies before the systems are put into use.

This paper presents a neighboring-effect modeling (NBEM) method that combines physical principles for problem formulation with a data-driven approach for estimation of coefficients. NBEM captures the fundamental physical relationship between energy intensity parameters and melt pool size, while it adopts a meta-model to enable fast prediction. The proposed NBEM method is designed to be seamless and sensitive to scan strategy considerations, especially the scan path. Section 2 describes the theoretical derivation of the method. Section 3 introduces the experimental design for method realization and validation. The last case study uses the 4,957 in-situ melt pool measurement from the first experiment to build the model. The second experiment generates 4,700 data points based on different scan strategy to validate the model. Four cases studies are presented in Section 4 to compare and validate the

NBEM method from different perspectives. Section 5 mainly discuss the conclusion and future works.

2. NEIGHBORING-EFFECT MODELING METHOD FOR MELT POOL PREDICTION

This section introduces the neighboring-effect modeling (NBEM) method that uses scan strategy to predict melt pool size for each focal point. In addition to the current process setting of laser power and scan velocity, a neighboring-effect factor is introduced into the model which quantifies the impact from the scan path.

Melt pool size is believed highly correlated to the energy input on the powder. The major factors that control the melt pool size are laser power and scan velocity. Empirical studies reveal that increasing laser power or decreasing scan velocity can enlarge the melt pool [19, 20]. Although measurements can be slightly different for overhanging and non-overhanging areas, the general correlations between melt pool size and these processing parameters remain the same [8]. In literature, these two processing parameters are major input variables in melt pool data-driven predictive models, which can be represented as:

$$S = f(P, v) \tag{1}$$

where the output S represents melt pool size, which can be melt pool width, length, or area. Without losing generality, this study uses melt pool area as the NBEM model output. Parameters P and v are laser power and scan velocity respectively. Equation (1) is usually used to study single track melt pool formation problem, which assumes a constant P and v and defines S as the average melt pool size of a scan track.

For a multi-track or 3d L-PBF build, scan pattern and tool-path are essential components of a scan strategy but are either missing or over-simplified in existing melt pool predictive model. Studies indicate that melt pool size and material properties present large variations for different scan patterns [21-23]. Hatch distance is a simplified form of scan pattern. Equation (1) transforms to a more accurate representation after adding hatch distance into consideration:

$$S = f(P, v, h) \tag{2}$$

Where parameter h is hatch distance. The output S, after transformation, represents the melt pool size of one melting track. With this update, the model can represent melt pool formation of multi-track scans separated by a constant hatch distance. However, Equation (2) needs further improvement for solving more complex L-PBF problems. Both empirical and simulated results indicate that scan direction and tool-path could significantly increase the uncertainty of melt pool formation even with a fixed hatch distance [24, 25]. In fact, the models built for either single track or multiple uniformed tracks, using Equation (1) or (2), cannot predict melt pool geometry for a real 3d build.

In a typical L-PBF process targeted for production, the tool-path is usually much more complicated than a uniform track pattern. Figure 1(a) and Figure 1(b) show two scan strategies using vertical serpentine scan pattern. While the same laser

power and scan velocity used, hatch distance can sufficiently declare the differences in the melt pool sizes. A smaller hatch distance provides powder more energy input due to more melting tracks and longer processing time. Hatch distance as a standalone variable can account for the difference between (a) and (b) based on Equation (2). However, although (c) has the same hatch spacing as (a), it is considered as a different scan pattern. The diagonal serpentine tool-path in (c) pre-scans the border so that the laser would turn off when moving between tracks. The laser beam in (d) moves in a spiral clockwise direction and concentrates to the center. (e) and (f) use the 'island' strategy where each 'island' employs either a serpentine or a spiral pattern. As a result, it is challenging to use only hatch distance to justify the different impacts of these scan strategies. To address this issue, melt pool predictive models require a better representation of scan strategy.
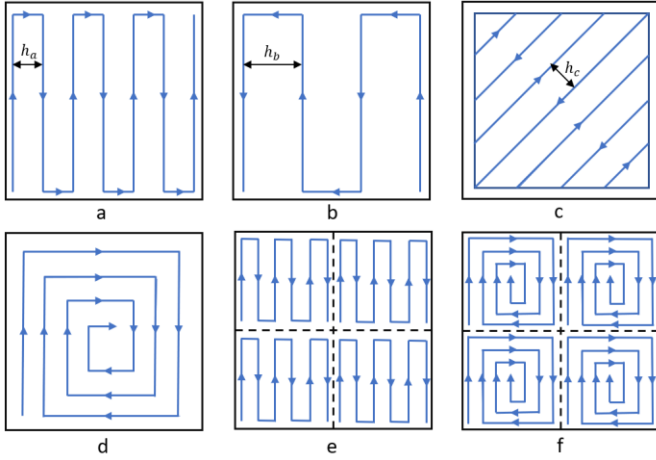

Figure 1. Examples of different scan strategies. (a) and (b) are the vertical serpentine pattern with hatch distance h_a and h_b. (c) is the orthogonal serpentine pattern with pre-scanned border, where $h_c = h_a$. (d) is the clockwise spiral centering pattern. (e) and (f) are the 'island' scanning strategy that each 'island' using serpentine or spiral pattern

To address this issue, a neighboring-effect vector is introduced to replace the original variable – hatch distance. This hypothesis is built upon the theory of laser irradiated area [26]. Spattered particles and metallic jets were observed around the melt pool, which could affect future melt pool formation in those areas. The former melted tracks irradiate the thermal energy to nearby powders, which potentially change the initial conditions of future melt pool formation. Such changes include the deviation of material properties and the preheating conditions [26]. Moreover, the initial conditions of melt pool formation are eventually changed when overlapping occurs [27]. As a result, besides the current energy input, a melt pool is sensitive to the melting history, including the distance and time to the previous melted areas. Equation (3) is the function after introducing the neighboring-effect factor.

$$S_i = f(P_i, v_i, \Omega_i) \tag{3}$$

where S_i is the melt pool area of the current focal point i. P_i and v_i are the laser power and scan velocity for this point. Ω_i is a matrix composes the processing parameters of the neighboring points for point i.

$$\Omega_i = \begin{bmatrix} P_{i1} & v_{i1} & \Delta t_{i1} & \Delta d_{i1} \\ P_{i2} & v_{i2} & \Delta t_{i2} & \Delta d_{i2} \\ & & \vdots & \\ P_{ij} & v_{ij} & \Delta t_{ij} & \Delta d_{ij} \end{bmatrix} \tag{4}$$

Where P_{ij} and v_{ij} are the laser power and scan velocity of the j_{th} neighboring point. They construct the basic impact from the neighboring points. Parameter Δt_{ij} and Δd_{ij} are the time and Euclidean distance between focal point i and former point j that used to scale the basic impact. The total number of elements in Ω_i varies, depending on the focal point location and the tool-path. Points near the edge have a smaller sized Ω matrix than inside points. And at the beginning of a process, matrix Ω is relatively small since there is limited amount of historical focal points.
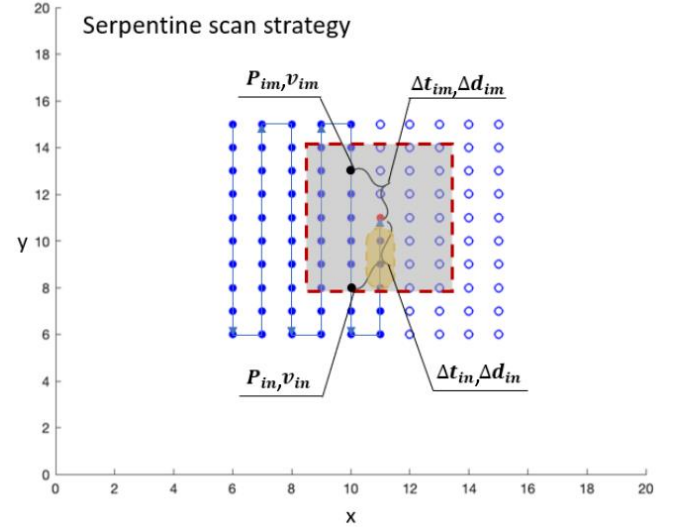

Figure 2. Neighboring points in serpentine scan strategy

Figure 2 shows an example of constructing a Ω matrix. Red, solid blue, and unfilled blue points represent current, previous, and future focal points, respectively. The arrow marks the scan direction of the serpentine scan strategy. The grey area is the neighboring-effect zone that enclosed by red dashed line. This study sets the zone as a $0.1mm \times 0.1mm$ square. The solid blue points on the grey area are the neighboring points to be included in the Ω matrix. In this work, the points located on the same straight track of current focal point is not included in the matrix (dashed yellow area) to avoid over-estimation. The dashed yellow area is considered a single track problem which is already covered by the P_i and v_i in Equation (3). Parameters P_{im}, v_{im}, P_{in}, v_{in} are the laser power and scan velocity associate to point m and point n, respectively. Δt_{im} and Δd_{im} are the time and distance difference between former point m and current point i. Similarly, Δt_{in} and Δd_{in} are assigned to point n. In this example, $\Delta t_{im} > \Delta t_{in}$ because the laser beam visit point m

Copyright © 2019 ASME

later than point n. However, $\Delta d_{im} < \Delta d_{in}$ since point n has shorter Euclidean dista. Collecting the variables for all neighboring points facilitates the formulation of the Ω_i for the current focal point i.

With Ω_i formulated, melt pool area can be expressed as a function of processing parameters and processing history. The smallest Ω_i is an empty matrix which is assigned to the first focal point on a tool-path since no previous points exist at that moment. Points in inner areas usually have larger Ω_i than those located on the edge.

The problem space of Equation (3) is very large. However, it is not necessary to calculate the effect of every single historic point if the cumulative impact can be estimated. As a result, Equation (5) summarizes a way to define the cumulative effect of previous scan points as a function of both time and distance. To avoid division by zero, both P_{ij} and v_{ij} are rescaled to 0.5 to 1.

$$f(\Omega_i) = \begin{bmatrix} P_{i1}/v_{i1} \\ P_{i2}/v_{i2} \\ \vdots \\ P_{ij}/v_{ij} \end{bmatrix}^T \begin{bmatrix} f_{\Delta t}(\Delta t_{i1}) & f_{\Delta d}(\Delta d_{i1}) \\ f_{\Delta t}(\Delta t_{i2}) & f_{\Delta d}(\Delta d_{i2}) \\ \vdots & \vdots \\ f_{\Delta t}(\Delta t_{ij}) & f_{\Delta d}(\Delta d_{ij}) \end{bmatrix} \qquad (5)$$

$\theta_i^{\Delta t}$ and $\theta_i^{\Delta d}$ represent the integrated factor of $f(\Omega_i)$ on time and distance perspective. In Equation (6) and (7), the input laser power P_{ij} of the neighboring point j provides a fundamental impact. Function $f_{\Delta t}(\Delta t_{ij})$ and $f_{\Delta d}(\Delta d_{ij})$ are used to scale the neighboring-effect from 0 (no impact) to 1 (strongest impact). Points geometrically and/or temporally remoted to the current focal point are scaled to have minimal impact.

$$\theta_i^{\Delta t} == \sum_{j=1}^{j=n} f_{\Delta t}(\Delta t_{ij}) \frac{P_{ij}}{v_{ij}} \qquad (6)$$

$$\theta_i^{\Delta d} = \sum_{j=1}^{j=n} f_{\Delta d}(\Delta d_{ij}) \frac{P_{ij}}{v_{ij}} \qquad (7)$$

Δt_{ij} or Δd_{ij} can be too large to provide any impact since an irradiated area is limited by its size. $f_t(\Delta t_{ij})$ and $f_d(\Delta d_{ij})$ represent the scaling functions of time lapse and distance, respectively.

The time-neighboring-effect focuses on modeling the preheating conditions of the current focal point, which depends on powder cooling rate. The cooling rate can affect the initial temperature of melting. The literature indicates the temperature of the focal point decreases quickly at the beginning but the total time for cooling and irradiated area can be varied [28, 29]. In this work, the time-neighboring-effect is formulated exponentially:

$$f_t(\Delta t_{ij}) = a_1 e^{a_2 \Delta t_{ij}} \qquad (8)$$

where $f_t(0) = 1$ and $f_t(\Delta t_{max}) = 0$. The parameters a_1, a_2 and Δt_{max} can be derived from experiments.

The distance-neighboring-effect aims to formulate the spatial impact such as spattering and denuded powder. Simulation and experimental results indicate the denuded width of an irradiated area is ranged from 0.04mm to 0.06mm for high-resolution scanning [26, 30]. The distance-neighboring-effect is formulated as:

$$f_d(\Delta d_{ij}) = b_1 e^{b_2 \Delta d_{ij}} \qquad (9)$$

where $f_d(0) = 1$ and $f_d(\Delta d_{max}) = 0$. Optimal coefficient b_1 and b_2 will be determined by experimental data. Δt_{max} and Δd_{max} equal to 20 ms and 0.6 mm in this study.

The coefficients in Equation (8) and (9) depend on the characteristics of L-PBF process. The neighboring-effect factor, $\theta_i^{\Delta t}$ and $\theta_i^{\Delta d}$ are summarization of all the individual effects from previous scan points. The general form of the melt pool predictive model can be expressed as:

$$S_i = f(P_i, v_i, \theta_i^{\Delta t}, \theta_i^{\Delta d}) \qquad (10)$$

After this transformation, the simplified model has four input variables where each variable linearly correlates to the output. Polynomial regression method is deployed in this work to build the NBEM model to avoid potential overfitting due to noisy data.

3. EXPERIMENTAL DESIGN

The experiments were conducted on the Additive Manufacturing Metrology Testbed (AMMT) at National Institute of Standards and Technology (NIST). The AMMT [31] is a fully customized metrology instrument that enables flexible control and measurement of the L-PBF process. An in-house developed AM software (SAM), which is capable of stereolithography (STL) slicing, scan path planning, G-code generation and interpretation [32], was used to program the different scan strategies for the experiment. Inconel 625 powder and substrate were used, the substrate has a dimension of 4" x 4" x 0.5". Twelve rectangular parts (with chamfered corners) of dimensions 10 mm x 10 mm x 5 mm were laid on the substrate, with a minimum spacing of 10 mm between parts. Each part was built with a different scan strategy. The melt pool was monitored by a high-speed camera which is optically aligned with the heating laser, such that the image of the melt pool is maintained stationary within the camera's field of view. The camera was triggered at every 200 μs (i.e. 2000 frames per second), with an integration time of 20 μs.
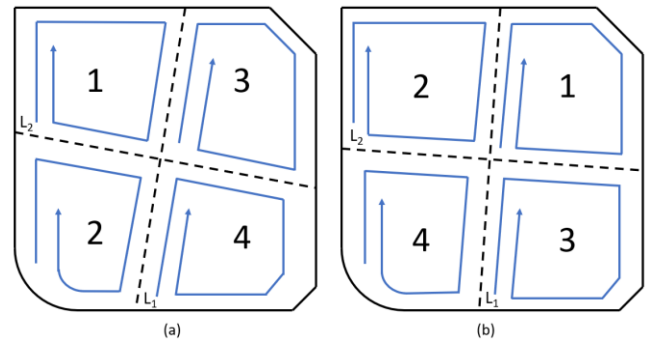

Figure 3. Scan strategy of the experiment. The number indicates the building order. (a) is the strategy for the first experiment and (b) is for the second experiment

The experiments apply the 'island' spiral concentrating scan strategy to both parts. Figure 3 shows the scan strategy for each

experiment. Both experiments divide the part into four islands by central lines L_1 and L_2, with vertical intersected. The intersection angle between L1 and the bottomline are 79 degrees and 87 degrees for (a) and (b), respectively. The laser scans each island spirally following the numbering order. The term 'track' for this scan strategy represents the straight scanning line between two infections. In these experiments, the laser accelerates at the beginning of each track until it reaches a nominal velocity and slows down when approaching the end of each track and before smoothly turning in a new direction. The laser power changes corresponding to the scan velocity changes. In general, a higher velocity goes with decreased power and lower velocity pairs with increased power. To avoid re-melting, there is no energy input from the laser when moving over a solidified area.

The G-Code is developed to specify the motion of the Galvo scanner of the L-PBF system. It is transformed to a time series of scanner positions and laser power as control commands. The scan velocity and focal point distance are calculated based on the focal point position and the associated time stamp. The first experiment uses 252,724 processing data points to scan the layer and the second experiment uses 238,871. Note, the processing parameters are the control command to build AM part which is not experimental data. The time interval between two commands is 10 µs. The average speed approximates the scan velocity at each focal point over the last two time intervals. Figure 4 shows the value maps of the simplified energy density term (P/v) of the applied scan strategy. The average laser power and the average scan velocity are 178 W and 667 mm/s respectively.
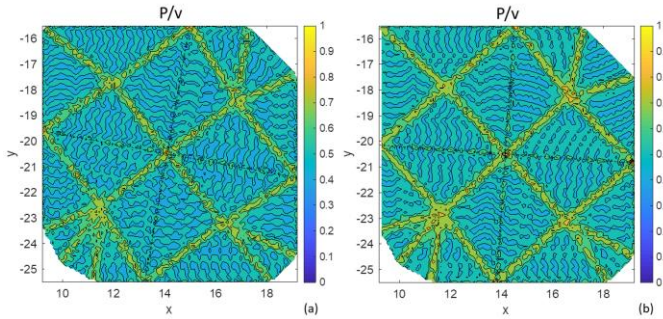

Figure 4. The value maps of P/v

A high-speed co-axial camera captures the melt pool at the focal point every 500 µs. The two experiments collect 4,957 and 4700 melt pool images. Figure 5 shows an example of the melt pool images. The image uses grayscale from 0 (black) to 255 (white). The brighter area in the image corresponds to a higher temperature range. Two threshold values of greyscale, 80 and 150, are used for melt pool edge detection. In this study, the melt pool boundary is approximated by an ellipse using least square fit. Figure 5(a) shows the edge detected using a threshold value of 150. Parameter 'a' represents the major radius of the ellipse which equals to ½ of the melt pool length. Parameter 'b' represents the minor radius which equals to ½ of the melt pool width. The melt pool area is measured by the ellipse area, which is about 0.0240 mm^2 in Figure 5(a). Lower threshold values

usually result in larger measurements of the melt pool area. In Figure 5(b), the melt pool area is measured about 0.031 mm^2. This study selects threshold value 150 since the corresponding melt pool area measurements agree better to the manual measurements.
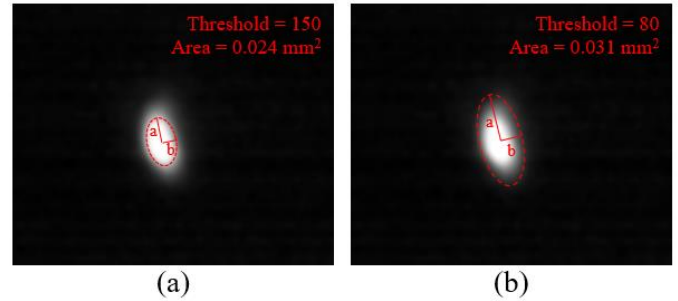

Figure 5. A melt pool image taken near the island center by the high-speed co-axial camera. (a) and (b) show the geometry measurements based on two different boundary grey scale threshold values. And the melt pool can be approximated by elliptic shapes. (a) A smaller melt pool area due to a higher threshold 150. (b) A larger melt pool area when using lower threshold 80

Figure 6 shows the contour and 3d surface of the measured melt pool area for the first experiment. Compared with Figure 4, overall, the melt pool size is found to be highly correlated with the focal point energy density. However, the melt pool sizes of the island centers are significantly higher than the change of energy density, which actually correlates very well with the concentrating scan pattern instead of the applied energy intensity. In addition, the part center and other places with higher energy density match the experimental measurement. As shown in Figure 7, the regional mean of each island is around 0.0160 mm^2. However, the mean melt pool size at the local centers is ranged from 0.0206 mm^2 to 0.0232 mm^2, which is about 25% - 70% higher than the average. Here the local center is defined as an area located at the center of each island that encloses the last 60 measurements.
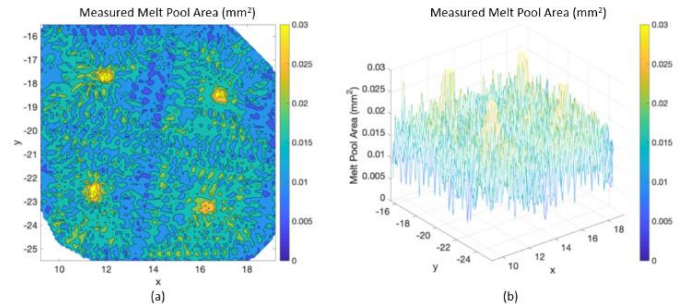

Figure 6. Measured melt pool area from the first experiment. (a) is the contour plot of measured melt pool area. (b) is the 3D surface plot of the melt pool area. The melt pool size varies from 0 (dark blue) to 0.03 (light yellow)
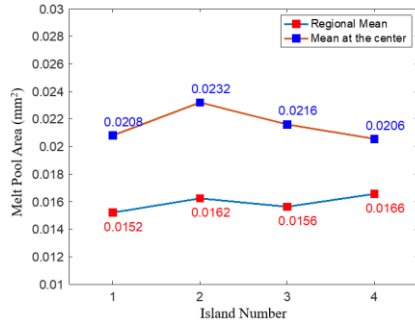
Figure 7. The measured mean value of the melt pool area for the 4 islands. The mean at the center of each island (last 60 measurement of each island) is significantly higher than the regional mean

4. CASE STUDIES

This section presents a comparison of four case studies. The first three case studies use 50% of the data from the first experiment to build the model and use the rest to validate the model. The fourth case study uses the data from the second experiment to validate the models built from the third case studies.

4.1 Power-velocity Model

The first case study simply apply the traditional power-velocity modeling method. The result provides the baseline to evaluate the other models. The polynomial regression method is deployed to fit the data with Equation (2) in the quadratic form:

$$S_i = c_1 + c_2 P_i + c_3 v_i + c_4 P_i v_i + c_5 P_i^2 + c_6 v_i^2 \qquad (11)$$

The original data, including the scan strategy and the melt pool measurement, is divided into a training dataset and a validation dataset by the ratio of 50% to 50%. The selected training data points are evenly distributed in the design space with no bias based on the Euclidean distance [33]. Table 1 lists the estimated coefficients fitted by the training dataset. Normalized root-mean-square error (NRMSE) is used as the validation criteria.

Table 1. Coefficient of the power-velocity model

	Estimate (10^{-6})
c_1	-3752.4528
c_2	149.3339
c_3	4.5426
c_4	-0.0532
c_5	-0.0368
c_6	-0.0061

Figure 8 shows the contour and 3d surface of the melt pool area prediction from the power-velocity model. Figure 9 shows the average predictive melt pool area for the global (entire island) that marked by blue and local (island center) that marked by read of each island. The numbers in the brackets are corresponding NRMSE of each island.

Compared to the actual measurement, the model fails to predict the irregular size of the melt pools at the island centers as it cannot distinguish the scan path impact.
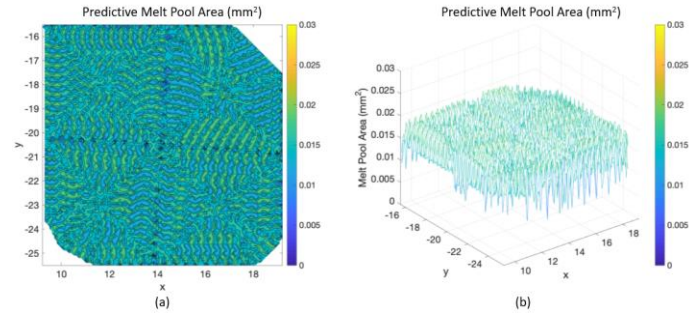

Figure 8. Contour (a) and 3d surface (b) of power-velocity model. Melt pool area is varied from 0 (dark blue) to 0.03 (light yellow)
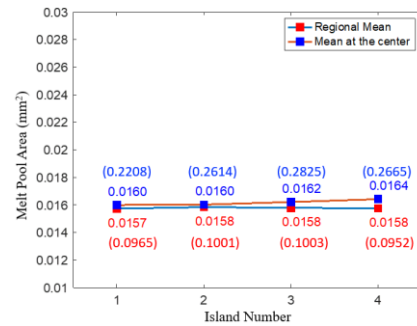

Figure 9. Comparative results of the melt pool area predicted by the power-velocity model. No significant difference observed between the regional means and the local center means. Local NRMSE is significantly higher than the global for all island.

4.2 Energy Density Model

Instead of having two independent input variables, this case study combines the laser power and scan velocity into one term (P/v) that can represent the energy density. The quadratic form of this model is:

$$S_i = c_1 + c_2 \left(\frac{P}{v}\right) + c_3 \left(\frac{P}{v}\right)^2 \qquad (12)$$

Table 2 lists the estimated coefficients of the energy density model. Figure 10 shows the contours and 3d surface of the model. The model can correlate to the variation of energy density. Figure 11 shows that the energy density model can slightly identify the irregular melt pool in the island center as the prediction in the center is generally higher than the entire island. However, it lacks of ability to provide accurate melt pool prediction as the NRMSE is still significantly higher than the actual measurement.

Table 2. Coefficient of the energy density model

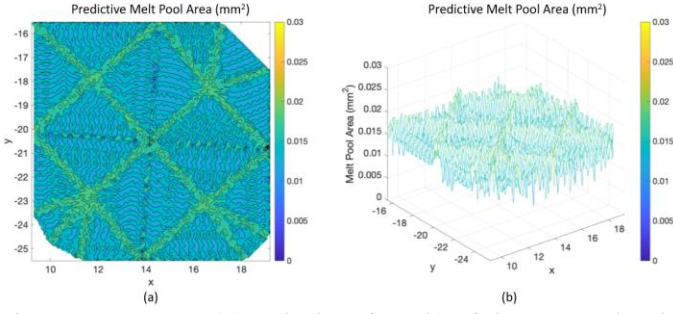|	Estimate (10^{-3})
c_1	-0.0510
c_2	73.3790
c_3	-60.5360

6

Copyright © 2019 ASME

Figure 10. Contour (a) and 3d surface (b) of the energy density model. Melt pool area is varied from 0 (dark blue) to 0.03 (light yellow)
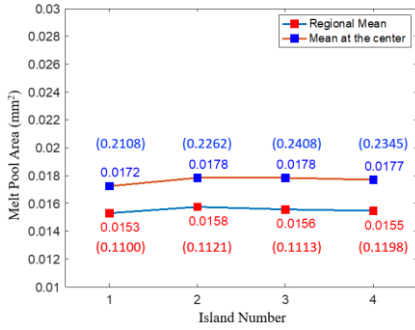

Figure 11. Comparative results of the melt pool area predicted by the energy density model. NRMSE is still significantly higher than global NRMSE though the model can slightly distinguish the difference of the melt pool in the island center

4.3 Global Performance of the NBEM Model

The same training and validation datasets are used in this case study. However, the power-velocity model is replaced by the NBEM model. The optimal coefficients of Equation (8) and (9) are identified with the training data. The exponential form of the time-neighboring-effect is:

$$f_t\left(\Delta t_{ij}\right) = e^{-0.00015\Delta t_{ij}} \quad (0 \le \Delta t_{ij} \le 20 \ ms) \quad (13)$$

Similarly, the distance-neighboring-effect function is:

$$f_t\left(\Delta d_{ij}\right) = e^{-7.941\Delta d_{ij}} \quad (0 \le \Delta d_{ij} \le 0.6 \ mm) \quad (14)$$

where $f_t\left(\Delta t_{ij} > 20 \ ms\right) = 0$ and $f_d\left(\Delta d_{ij} > 0.6 \ mm\right) = 0$. The neighboring-effect factor, $\theta_i^{\Delta t}$ and $\theta_i^{\Delta t}$, can be calculated through Equation (13) and (14) based on the corresponding laser power. The quadratic form of Equation (10) can be presented as:

$$S_i = c_1 + c_2 P_i + c_3 v_i + c_4 \theta_i^{\Delta t} + c_5 \theta_i^{\Delta d} + c_6 P_i v_i + c_7 P_i \theta_i^{\Delta t} + c_8 P_i \theta_i^{\Delta d} + c_9 v_i \theta_i^{\Delta t} + c_{10} v_i \theta_i^{\Delta d} + c_{11} \theta_i^{\Delta t} \theta_i^{\Delta d} + c_{12} P_i^2 + c_{13} v_i^2 + c_{14} \theta_i^{\Delta t} + c_{14} \theta_i^{\Delta d} \quad (15)$$

Table 3. Coefficients of the NBEM model for the four islands

	Estimated (10^6)		Estimated (10^6)
c_1	-52219.4786	c_9	-0.7939
c_2	813.1230	c_{10}	0.3374
c_3	172.3596	c_{11}	-6.1637
c_4	292.8705	c_{12}	1.7680
c_5	557.7027	c_{13}	-0.0973
c_6	-0.7981	c_{14}	8.7636
c_7	1.8801	c_{15}	-9.1009
c_8	1.3040		

Table 3 lists the estimated value of c_1 to c_{10}. Figure 12 shows the contour and 3d surface of the predicted melt pool area from the NBEM melt pool model. Different from the power-velocity model, the NBEM model can predict the local melt pool size change at the island centers. The general trend and irregularity of the melt pool size predicted from the model match the actual measurements shown in Figure 6.

As shown in Figure 13, the NBEM model can distinguish the irregular melt pool based on the scan path. The global and local NRMSE are relatively much lower than the power-velocity and energy density model. The average predictive melt pool in the island center also close to the actual measurement.
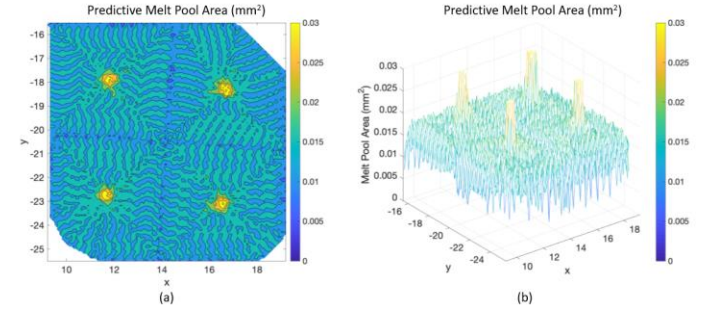

Figure 12. Contour (a) and 3d surface (b) of NBEM model. Melt pool area is varied from 0 (dark blue) to 0.03 (light yellow)
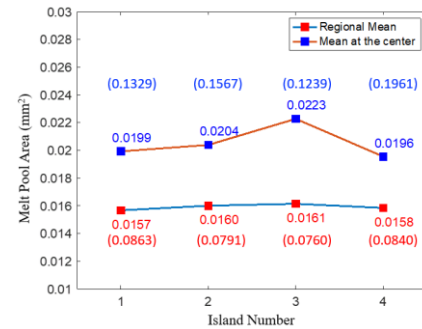

Figure 13. Comparative results of the melt pool area predicted by the NBEM model. The average predictive melt pool area at the local centers are predictively higher than the regional means. NRMSE (in the brackets) is reduced.

4.4 NBEM Model for Melt pool Prediction for a new scan strategy

The last case study uses the experimental data collected from the second experiment to validate the models built in the previous case studies. It assumes only the model and pre-designed scan strategy is available to the AM user without knowing any experimental data. Figure 14 maps the actual measurement for validation purpose in 2D contour and 3D surface. Figure 15 plots the average melt pool area for each island in the second experiment.
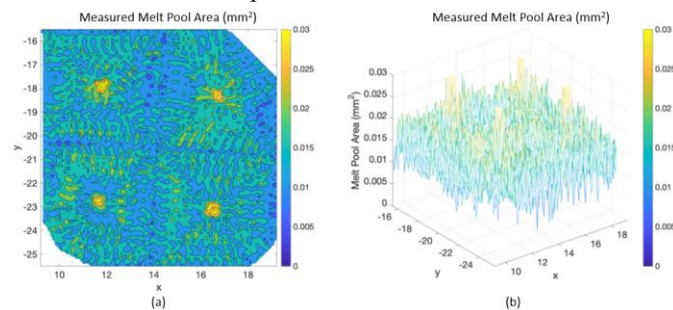

Figure 14. Contour (a) and 3d surface (b) of melt pool measurement of the second experiment. Melt pool area is varied from 0 (dark blue) to 0.03 (light yellow)
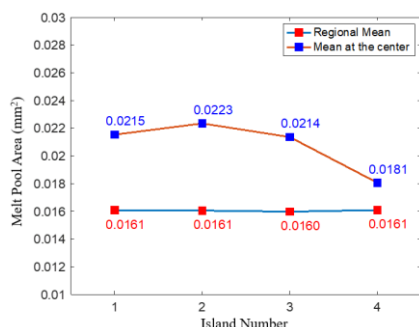

Figure 15. Average melt pool area that measured from the second experiment. The mean at the center is calculated from the last 60 measurement data to the island center

For comparison purpose, Figure 16 provides the contour plots of the predictive melt pool area of the second experiment from power-velocity (a) and energy density model (b). Similarly, to previous case studies, both models fail to predict the irregular melt pool located in the island center.
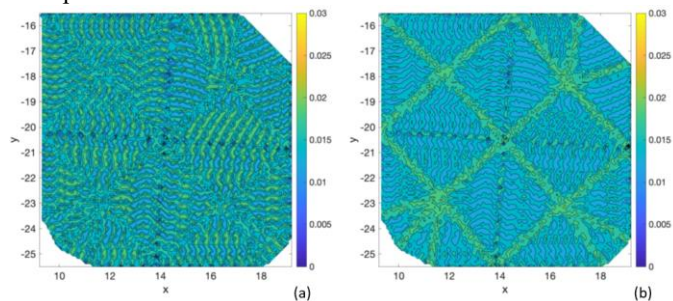

Figure 16. Contour plot of the predictive melt pool area. (a) is the result derived from the power-velocity model. (b) is from the energy density model
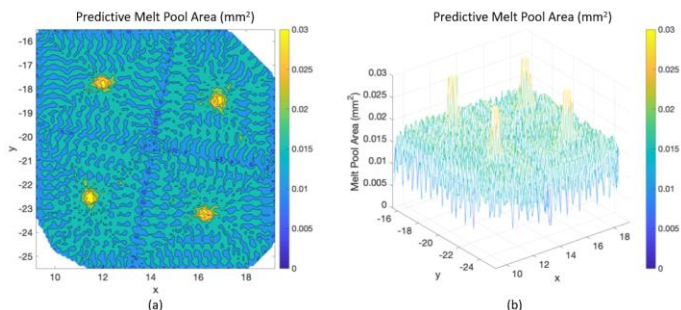

Figure 17. Contour and 3d surface of the predictive melt pool area for the scan strategy in the second experiment using the NBEM model created in the third case study.

Figure 18 plots the detail of the predictive results of each island in the second experiment. As shown, the model developed previously can still provide reliable prediction to the new experiment.
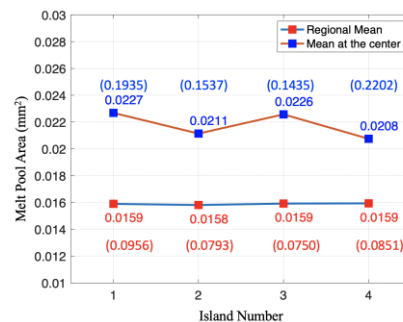

Figure 18. Comparative results of the melt pool area predicted by the NBEM model. Numbers in the brackets are the NRMSE of each island and island center

5. DISCUSSION

The objective of this work is to explore a modeling methodology tailored for L-PBF melt pool size prediction to evaluate different scan strategies. The fundamental challenge is the difficulty of formulating a universal method with minimum input variables but sufficiently representing various scan patterns and tool-paths. Current physics-based models such as FEA and CFD are limited by either high computational cost or difficulties in convergence. This work addresses this challenge by introducing the NBEM method to incorporate the cumulative impact from neighboring historical points as model input. The contributions from the past scan points and process parameters to the cumulative impact are weighed based on the distance and time lapse between the previous scan points and the current focal point. Hence the model is universal for most scan patterns.

The NBEM method allows L-PBF users to evaluate the melt pool geometry resulted from various scan strategies based on computational cost-effective predictive models trained with experimental data. The NBEM model can improve the irregular melt pool prediction for more than 50% for each island based on the scan strategy. Quantification of the impact from scan pattern is difficult to be obtained through traditional power-velocity models. As shown in the first and the third case studies,

compared to the power-velocity model, the NBEM model can reduce the global NRMSE for about 20% from 0.10 to 0.08. More importantly, the local NRMSE of the island center is reduced for about 50%. The last case study mimics the more realistic conditions when the new scan strategy is posted without any experimental data. The model approves the NBEM can work properly when applying new scan strategy.

Both the computational cost for the training part and that of the prediction part using NBEM method are substantially lower than traditional FEA and CFD methods. The polynomial formed NBEM model can be established in seconds from thousands of data points. The prediction can be done almost instantly. This advantage enables the NBEM method as a potential solution for real time closed-loop control of L-PBF processes.
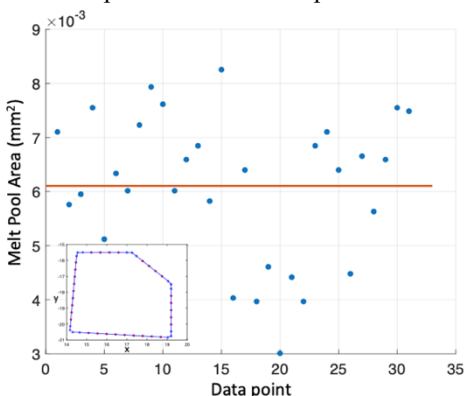

Figure 19. Melt pool measurement located on the edge of the first island. Figure in the bottom left is the scan path. Blue dots are the melt pool measurement data points. The red line is them mean value of these data point

Despite these advantages, the proposed method remains at its early development stage. Basically, the method was only validated by a single layer experiment. The impact from previous layers, overhanging features, and more complex thermal conditions are not covered by the current method yet. Questions such as "can the method provide reliable melt pool prediction for the whole part of a 3d build" require further investigation. Furthermore, it is not clear how the method performs for more complex scan patterns. For example, it is important to know the sensitivity of the method to island size, scan direction, or energy input. It is possible the performance of the method will decrease when island is too small, or the energy input exceeds some threshold values.

Another issue comes from the experiment design. The melt pool measurement itself contains uncertainties, which may affect the prediction accuracy of the NBEM model. Figure 19 marks the measured melt pool area on the edge of the first island in the second experiment. The red line is the average melt pool area. Since the melt pool in this area receives minimum impact from neighboring points, it is reasonable to assume that the melt pool size on the contour is independent of the neighboring-effect. The bottom left corner plots the scan path. Only the red solid dots are included in the scattering plot as they are formulated by similar laser power (104.96-105.02 W) and scan velocity (899.92-

900.20 mm/s). As shown in the figure, the melt pool area observed has a large variation. It can be an accumulative uncertainty from the initial uncertainty of powder particle size, or the approximation of the melt pool measurement as explained in Figure 5 as uncertainty play significant role in the predictive accuracy of such L-PBF models [34, 35]. The initial experimental data contains some noise generated by intrinsic or extrinsic uncertainties. The model developed in Section 4.3 and 4.4 are assumed to be an ideal model without any noise.

The noise introduced by the measurement uncertainty can be potentially reduced by improving the measurement method. For example, instead of using ellipse approximation, the melt pool can be measured directly from pixel values. This approach is assumed to be more accurate for irregular shaped melt pool. The effect of the uncertainty may also be reduced if more appropriate threshold values are used. In this work, two threshold values are investigated. Future work may find the optimal threshold value between 150 and 80.

In summarize, this work introduces a predictive modeling method to improve the melt pool predictability by incorporating scan strategies as inputs beyond the traditional input variables of laser power and scan speed. About 2,500 melt pool measurement data from the first experiment are used to construct the model. The second experiment applies a different scan strategy and generates a new dataset with 4,700 data points to validate the previously developed model. The validation result indicates that the NBEM modeling method has the highest accuracy with the lowest NRMSE compared to the other traditional modeling methods. It is also the only model can correctly point out the center of each island contain irregular melt pool size clusters.

However, though the NBEM method has verified for this LPBF system for the given material, it cannot guarantee the model works for other machines. To the best of the authors' knowledge, there is no universal melt pool predictive model can accurately predict the melt pool size under the conditions mentioned above. The authors' previous studies investigate the differences between different AM conditions. The findings indicate even slight changes such as increasing the particle size of metal powder can significantly affect the melt pool formation. Uncertainty is still the biggest challenge in the AM community, where this research aims to improve the current state of the art of metal additive manufacturing. However, based on the proposed approach, the AM machine manufacturers can characterize their systems for various conditions and derived a library of predictive models, which can be used to generate the machine and material specific best scan strategies and process parameter settings.

DISCLAIMER

authors and do not necessarily reflect the views of NIST or any other supporting U.S. government or corporate organizations.

ACKNOWLEDGMENTS

REFERENCES

[1] King, W. E., Anderson, A. T., Ferencz, R., 2015, "Laser Powder Bed Fusion Additive Manufacturing of Metals; Physics, Computational, and Materials Challenges," Applied Physics Reviews, 2(4) pp. 041304.

[2] Lu, Y., Choi, S., and Witherell, P., 2015, "Towards an integrated data schema design for additive manufacturing: Conceptual modeling," ASME 2015 International Design Engineering Technical Conferences and Computers and Information in Engineering Conference, Anonymous American Society of Mechanical Engineers, pp. V01AT02A032-V01AT02A032.

[3] Witherell, P., Feng, S., Simpson, T. W., 2014, "Toward Metamodels for Composable and Reusable Additive Manufacturing Process Models," Journal of Manufacturing Science and Engineering, 136(6) pp. 061025.

[4] Cunningham, R., Narra, S. P., Montgomery, C., 2017, "Synchrotron-Based X-Ray Microtomography Characterization of the Effect of Processing Variables on Porosity Formation in Laser Power-Bed Additive Manufacturing of Ti-6Al-4V," Jom, 69(3) pp. 479-484.

[5] Tang, M., Pistorius, P. C., and Beuth, J. L., 2017, "Prediction of Lack-of-Fusion Porosity for Powder Bed Fusion," Additive Manufacturing, 14pp. 39-48.

[6] Khairallah, S. A., Anderson, A. T., Rubenchik, A., 2016, "Laser Powder-Bed Fusion Additive Manufacturing: Physics of Complex Melt Flow and Formation Mechanisms of Pores, Spatter, and Denudation Zones," Acta Materialia, 108pp. 36-45.

[7] Rai, R., Elmer, J., Palmer, T., 2007, "Heat Transfer and Fluid Flow during Keyhole Mode Laser Welding of Tantalum, Ti–6Al–4V, 304L Stainless Steel and Vanadium," Journal of Physics D: Applied Physics, 40(18) pp. 5753.

[8] Lu, Y., Yang, Z., Eddy, D., 2018, "Self-Improving Additive Manufacturing Knowledge Management," ASME 2018 International Design Engineering Technical Conferences and Computers and Information in Engineering Conference, Anonymous American Society of Mechanical Engineers, pp. V01BT02A016-V01BT02A016.

[9] Thijs, L., Verhaeghe, F., Craeghs, T., 2010, "A Study of the Microstructural Evolution during Selective Laser Melting of Ti–6Al–4V," Acta Materialia, 58(9) pp. 3303-3312.

[10] Lopez, F., Witherell, P., and Lane, B., 2016, "Identifying Uncertainty in Laser Powder Bed Fusion Additive Manufacturing Models," Journal of Mechanical Design, 138(11) pp. 114502.

[11] Zhang, B., Dembinski, L., and Coddet, C., 2013, "The Study of the Laser Parameters and Environment Variables Effect on Mechanical Properties of High Compact Parts Elaborated by Selective Laser Melting 316L Powder," Materials Science and Engineering: A, 584pp. 21-31.

[12] Mertens, R., Dadbakhsh, S., Van Humbeeck, J., 2018, "Application of Base Plate Preheating during Selective Laser Melting," Procedia CIRP, 74pp. 5-11.

[13] Yan, W., Smith, J., Ge, W., 2015, "Multiscale Modeling of Electron Beam and Substrate Interaction: A New Heat Source Model," Computational Mechanics, 56(2) pp. 265-276.

[14] Yan, W., Ge, W., Smith, J., 2016, "Multi-Scale Modeling of Electron Beam Melting of Functionally Graded Materials," Acta Materialia, 115pp. 403-412.

[15] Yan, W., Ge, W., Smith, J., 2015, "Towards high-quality selective beam melting technologies: modeling and experiments of single track formations," 26th Annual international symposium on solid freeform fabrication, Austin, Texas, Anonymous .

[16] King, W., Anderson, A., Ferencz, R., 2015, "Overview of Modelling and Simulation of Metal Powder Bed Fusion Process at Lawrence Livermore National Laboratory," Materials Science and Technology, 31(8) pp. 957-968.

[17] Yang, Z., Eddy, D., Krishnamurty, S., 2017, "Investigating Grey-Box Modeling for Predictive Analytics in Smart Manufacturing," ASME 2017 International Design Engineering Technical Conferences and Computers and Information in Engineering Conference, Anonymous American Society of Mechanical Engineers, pp. V02BT03A024-V02BT03A024.

[18] Gibson, I., Rosen, D.W., and Stucker, B., 2010, "Additive manufacturing technologies," Springer, .

[19] Gong, H., Gu, H., Zeng, K., 2014, "Melt pool characterization for selective laser melting of Ti-6Al-4V pre-alloyed powder," Solid freeform fabrication symposium, Anonymous pp. 256-267.

[20] Khan, M., Romoli, L., Fiaschi, M., 2010, "Experimental Investigation on Laser Beam Welding of Martensitic Stainless Steels in a Constrained Overlap Joint Configuration," Journal of Materials Processing Technology, 210(10) pp. 1340-1353.

[21] Beal, V., Erasenthiran, P., Hopkinson, N., 2006, "The Effect of Scanning Strategy on Laser Fusion of Functionally Graded H13/Cu Materials," The International Journal of Advanced Manufacturing Technology, 30(9-10) pp. 844-852.

[22] Islam, M., Purtonen, T., Piili, H., 2013, "Temperature Profile and Imaging Analysis of Laser Additive Manufacturing of Stainless Steel," Physics Procedia, 41pp. 835-842.

[23] Carter, L. N., Martin, C., Withers, P. J., 2014, "The Influence of the Laser Scan Strategy on Grain Structure and Cracking Behaviour in SLM Powder-Bed Fabricated Nickel Superalloy," Journal of Alloys and Compounds, 615pp. 338-347.

[24] Kamath, C., El-dasher, B., Gallegos, G. F., 2014, "Density of Additively-Manufactured, 316L SS Parts using Laser Powder-Bed Fusion at Powers Up to 400 W," The International Journal of Advanced Manufacturing Technology, 74(1-4) pp. 65-78.

[25] Parry, L., Ashcroft, I., and Wildman, R. D., 2016, "Understanding the Effect of Laser Scan Strategy on Residual Stress in Selective Laser Melting through Thermo-Mechanical Simulation," Additive Manufacturing, 12pp. 1-15.

[26] Furumoto, T., Egashira, K., Munekage, K., 2018, "Experimental Investigation of Melt Pool Behaviour during Selective Laser Melting by High Speed Imaging," CIRP Annals, .

[27] Gong, H., Rafi, K., Gu, H., 2014, "Analysis of Defect Generation in Ti–6Al–4V Parts made using Powder Bed Fusion Additive Manufacturing Processes," Additive Manufacturing, 1pp. 87-98.

[28] Manvatkar, V., De, A., and DebRoy, T., 2014, "Heat Transfer and Material Flow during Laser Assisted Multi-Layer Additive Manufacturing," Journal of Applied Physics, 116(12) pp. 124905.

[29] Bertoli, U. S., Guss, G., Wu, S., 2017, "In-Situ Characterization of Laser-Powder Interaction and Cooling Rates through High-Speed Imaging of Powder Bed Fusion Additive Manufacturing," Materials & Design, 135pp. 385-396.

[30] Hooper, P. A., 2018, "Melt Pool Temperature and Cooling Rates in Laser Powder Bed Fusion," Additive Manufacturing, 22pp. 548-559.

[31] Lane, B., Mekhontsev, S., Grantham, S., 2016, "Design, developments, and results from the nist additive manufacturing metrology testbed (ammt)," Solid Freeform Fabrication Symposium, Austin, TX, Anonymous pp. 1145-1160.

[32] Yeung, H., Lane, B., Donmez, M., 2018, "Implementation of Advanced Laser Control Strategies for Powder Bed Fusion Systems," Procedia Manufacturing, 26pp. 871-879.

[33] Yang, Z., Eddy, D., Krishnamurty, S., 2016, "Investigating predictive metamodeling for additive manufacturing," ASME 2016 International Design Engineering Technical Conferences and Computers and Information in Engineering Conference, Anonymous American Society of Mechanical Engineers, pp. V01AT02A020-V01AT02A020.

[34] Moges, T., Ameta, G., and Witherell, P., 2019, "A Review of Model Inaccuracy and Parameter Uncertainty in Laser Powder Bed Fusion Models and Simulations," Journal of Manufacturing Science and Engineering, 141(4) pp. 040801.

[35] Moges, T., Yan, W., Lin, S., 2018, "Quantifying Uncertainty in Laser Powder Bed Fusion Additive Manufacturing Models and Simulations," Solid Freeform Fabrication Symposium An Additive Manufacturing Conference.

Copyright © 2019 ASME